How to cite: Angew. Chem. Int. Ed. 2023, e202302781
doi.org/10.1002/anie.202302781

Fluorescent Probes

Photoactivatable Carbo- and Silicon-Rhodamines and Their Application in MINFLUX Nanoscopy

Ayse Aktalay[+], Taukeer A. Khan[+], Mariano L. Bossi, Vladimir N. Belov,* and Stefan W. Hell**

Abstract: New photoactivatable fluorescent dyes (rhodamine, carbo- and silicon-rhodamines [SiR]) with emission ranging from green to far red have been prepared, and their photophysical properties studied. The photocleavable 2-nitrobenzyloxycarbonyl unit with an alpha-carboxyl group as a branching point and additional functionality was attached to a polycyclic and lipophilic fluorescent dye. The photoactivatable probes having the HaloTagTM amine (O2) ligand bound with a dye core were obtained and applied for live-cell staining in stable cell lines incorporating Vimentin (VIM) or Nuclear Pore Complex Protein NUP96 fused with the HaloTag. The probes were applied in 2D (VIM, NUP96) and 3D (VIM) MINFLUX nanoscopy, as well as in superresolution fluorescence microscopy with single fluorophore activation (VIM, live-cell labeling). Images of VIM and NUPs labeled with different dyes were acquired and their apparent dimensions and shapes assessed on a lower single-digit nanometer scale. Applicability and performance of the photoactivatable dye derivatives were evaluated in terms of photoactivation rate, labeling and detection efficiency, number of detected photons per molecule and other parameters related to MINFLUX nanoscopy.

Introduction

Fluorescence microscopy allows visualizing the interior of cells and the interactions of their molecular components through fluorescence labeling. The diffraction resolution barrier of about half the wavelength of light, which hampered fluorescence microscopy throughout the 20th century, was ultimately broken by transiently preparing fluorophores closer than half the wavelength of light in different molecular states.[1] Specifically, toggling between non-fluorescent and fluorescent states is key to virtually all super-resolution fluorescence (nanoscopy) methods. MINFLUX nanoscopy,[2] a recent super-resolution technique relying on switchable or photoactivatable fluorophores, can routinely attain single-digit nanometer resolution. The yet more recent and related MINSTED concept[3] can localize fluorophores with 2–3 Å precision at room temperature.[3b] MINFLUX and MINSTED nanoscopy are particularly powerful with photoactivatable fluorophores that can be transferred from a "lasting" optically inert off-state into an on-state providing fluorescence emission upon irradiation with excitation light. While such photoactivatable markers provide irreversible off→on switching, photochromic fluorescent dyes or proteins afford reversible off↔on switching.[4] Both off-on transition types can be harnessed in MINFLUX nanoscopy, as well as in the widely established and popular single-molecule-localization microscopy (SMLM) methods.[5] The present study focuses on photoactivatable ("caged") dyes which can be transformed from a non-emissive to an emissive state under irradiation with UV or violet light (365 nm–405 nm). The activated dye emits light in the form of fluorescence upon excitation with visible light.[6] The sequence of activation and excitation events offers the possibility of highlighting the defined regions of space ("light injections") at given time intervals. Our photoresponsive molecular switches are thus invaluable not only for super-resolution microscopy, but also for tracking fluorophores and observing molecular dynamics in living matter.

Our study is motivated by the fact that photoactivatable synthetic dyes typically emit much higher numbers of photons than fluorescent proteins. Their activation (outcome, kinetics) by a photochemical reaction depends on the chemical structure of the initial compound and affords controlled "turn-on" of spatially sparse individual molecules.[7] The color palette of photoactivatable dyes spans through the visible spectrum. Fortunately, small organic fluorophores can be prepared with diverse core structures, polarities,[6a] tailored spectral properties, and target specificities.[7] Yet advances in microscopy techniques

[*] Dr. A. Aktalay,[+] Dr. M. L. Bossi, Prof. Dr. S. W. Hell
Department of Optical Nanoscopy, Max Planck Institute for Medical Research (MPI-MR)
Jahnstraße 29, 69120 Heidelberg (Germany)
E-mail: Mariano.Bossi@mr.mpg.de

Dr. T. A. Khan,[+] Dr. V. N. Belov, Prof. Dr. S. W. Hell
Department of NanoBiophotonics, Max Planck Institute for Multidisciplinary Sciences (MPI-NAT)
Am Fassberg 11, 37077 Göttingen (Germany)
E-mail: vladimir.belov@mpinat.mpg.de
Stefan.Hell@mpinat.mpg.de

[+] These authors contributed equally to this work.

demand brighter, multifunctional fluorescent probes with tightly controlled photophysical properties. Although progress has been made by synthesizing caged fluorophores with negatively charged solubilizing groups,[6a] live-cell labeling requires cell-permeable probes (uncharged molecules) that retain their ability to specifically bind with proteins of interest (POIs) in living specimens.[8]

Results and Discussion

Design and synthesis

Here we report the design, synthesis and photoactivation of dyes (**1a–e** in Scheme 1) intended for specific staining in living and fixed cells. The variety of masked fluorescent dyes undergoing "clean" photoactivation (with minimal amounts of non-fluorescent by-products), suitable for intracellular targeting and applicable in MINFLUX nanoscopy is limited. This need motivated us to synthesize photoactivatable green-, yellow-, orange- and red-emitting dyes having rhodamine,[9a] carborhodamine[9b] and silicon rhodamine[9c] cores. The photocleavable 2-nitrobenzyloxycarbonyl groups attached to nitrogen atoms of xanthene fluorophores provide efficient quenching of the emission and clean recovery of the fluorescence signal upon photolysis.[6a,b,10,11] The negatively charged sulfonic acid groups attached to 2-nitrobenzyloxycarbonyl residues via linkers make the caged fluorophores water-soluble, but cell-impermeable.[6a] Unless these ionic solubilizing groups are present, the photoactivatable dyes remain hydrophobic, tend to aggregate and bind unspecifically to cell membranes and non-polar domains in bio specimens. The dye polarity can be increased and the solubility improved by adding a useful functionality to the caging group. We transformed the benzyl CH_2 groups to CHCOOH fragments and thus introduced two branching points and two versatile reactive centers. This approach enables to introduce not only carboxamides, but carboxylates with protection "orthogonal" to the ester groups in compounds **5** and **6** (Scheme 2). These modifications of caging moieties do not affect the spectral properties of the fluorophore, but lead to polar structures (amides) with improved solubility and biocompatibility. The branched structures have additional degrees of freedom (molecular rotations) which also increase solubility. This transformation was applied to the least soluble and most lipophilic dye **1a**.[6b,10] Dyes **1b–d** were found to provide cell permeability and specific labeling without modifications.

Q-SiR

First, we focused on the design of a photoactivatable analog of red-emitting Q-SiR (Q = quinoline) (**1a**), as Q-SiR was found to be a bright and photostable fluorophore excelling in superresolution microscopy.[6b,10] In previous work, we applied the photoactivatable Q-SiR probes in STED and MINSTED nanoscopy. However, due to its poor solubility and high lipophilicity, only dedicated methods for antibody labeling and purification were developed.[3,10] The absence of methoxy groups in the structure of 2-nitrobenzyloxycarbonyl "cage" in Q-SiR dye **1a** made it stable against two-photon activation with the intense 775 nm STED laser light, a condition required for STED and MINSTED. While this is irrelevant for MINFLUX imaging, low photoactivation rates provide better control of the activation of fluorophores in the microscope, reducing the probability of double-activated events. The presence of a bulky and rigid polycyclic rhod-

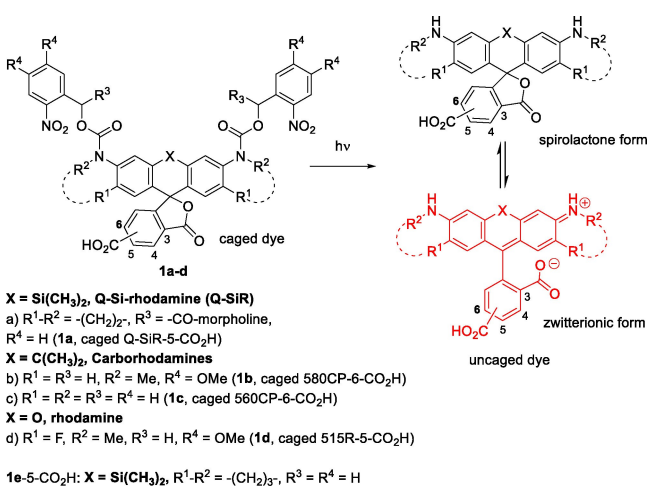

Scheme 1. Photoactivatable (caged) dyes and their photolysis to bright and photostable fluorescent products.

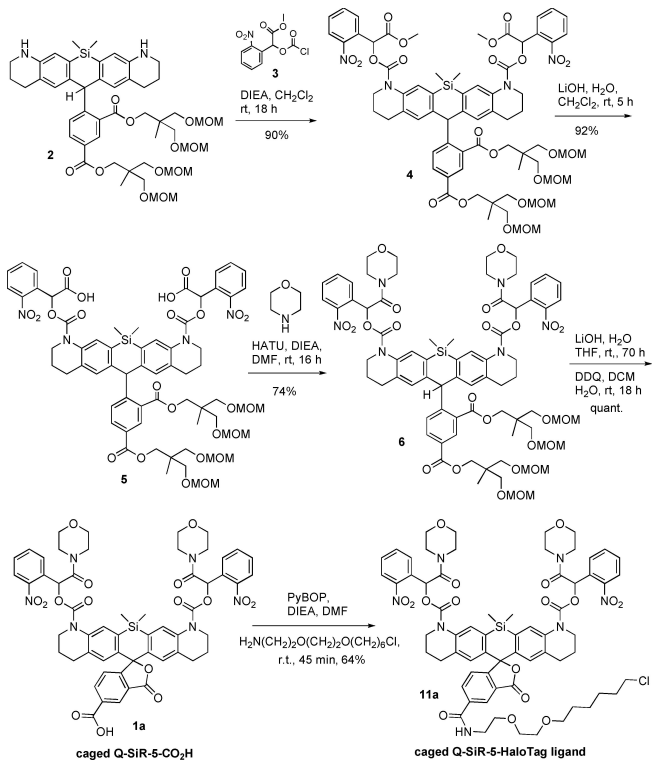

Scheme 2. Synthesis of photoactivatable Q-SiR-5-CO_2H and its conjugate with HaloTag™ amine (O2) ligand.

amine core in Q-SiR, in addition to two hydrophobic caging groups, poses a challenge in application of this dye in specific bio-labeling, especially in living cells. To overcome this problem, without compromising cell permeability, we attached the carboxylic acid group to the benzylic position of 2-nitrobenzyloxycarbonyl residue (compound **5**) and then prepared the polar carboxamide **6** (Scheme 2). The derivatization of *O*-(2-nitrobenzyl)carbamate caging groups attached to photoactivatable rhodamines has not been explored since 1998, due to synthetic challenges.[12] Here, we selected morpholine as the amide substituent, as it is known to increase the polarity and solubility of drugs, and the morpholine ring itself offers a well-balanced lipophilic-hydrophilic profile with desirable biocompatibility characteristics.[13]

To further demonstrate the advantages of the introduction of the branching points and the polar morpholide residues, we prepared model compound **1e** as a reference dye, caged with two 2-nitrobenzyl groups, but without morpholide groups. The difference in the hydrophilic character between **1a** and **1e** is remarkable, with a reduction of logP value (the octanol/water partition coefficient) of over 2 units for **1a** (Figure S1) introduced by the presence of morpholide groups. Moreover, a similar difference was observed for the corresponding HaloTag probes (**11a** and **11e** in Scheme 3).

The synthesis of the caged red-emitting Q-SiR (**1a**) is given in Scheme 2, and full experimental details—in Supporting Information. The leuco amine[9c,10] reacted with methyl 2-(2-nitrophenyl)mandelate chloroformate[14] to provide carbamate **4**. The *α*-carboxy-substituted [(2-nitrobenzyl)oxy]carbonyl residue is protected as methyl ester, which can be removed by saponification (aq. LiOH) to produce the free diacid **5** without destruction of the carbamate function. This important feature makes the synthesis more general as it allows to use various amines and couple them with diacid **5** as a common building block. In our case, the HATU mediated coupling reaction between diacid (**5**) and morpholine provided the required α-carboxamide-substituted carbamate **6**. The hydrolysis of both ester groups of leuco rhodamine **6** was challenging because this intermediate contains carbamate groups sensitive to basic hydrolysis and acidic CH protons activated by 3 electron withdrawing substituents (oxygen, carbonyl and 2-nitrophenyl). After screening and optimization of the reaction conditions (see Supporting Information), we managed to cleave both ester groups and oxidize the intermediate to the target acid **1a** in two steps and with nearly quantitative yield. The 5-carboxy isomer of the Q-SiR (**1a**) was used for bioconjugation with Halo-Tag™ fusion proteins (VIM and NUP96) in the form of amide **11a** (Scheme 2).

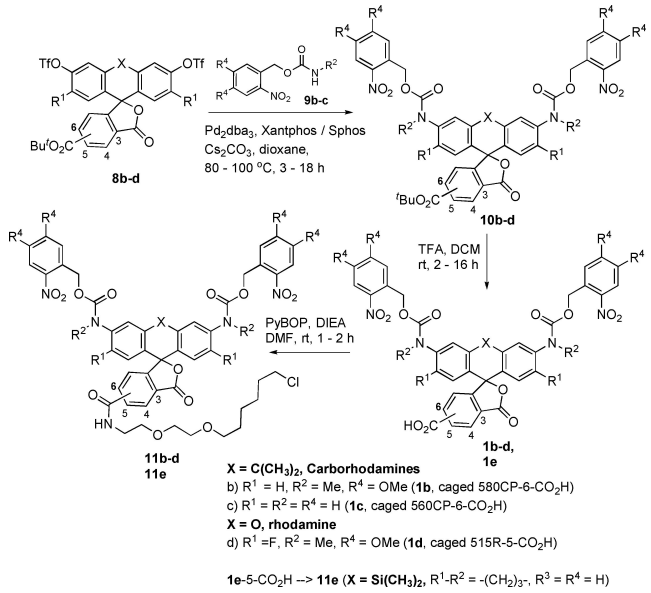

Scheme 3. Synthesis of photoactivatable 580CP, 560CP and 515R dyes and amides prepared from dyes **1b–e** and HaloTag™ amine (O2).

Photoactivatable Rhodamines (R) and Carborhodamines (CP) Emitting Green (515R), Yellow (560CP) and Orange (580CP) Light

For the synthesis of other photoactivatable compounds emitting at lower wavelengths than Q-SiR, we selected photostable dyes—rhodamine (515R), as well as carborhodamines 560CP and 580CP—well performing in STED and confocal microscopy of biological objects.[15] The free (non-conjugated) dye 515R emits at 543 nm, and free dyes 560CP and 580CP—at 588 nm and 607 nm, respectively (emission maxima). Other probes (**1b**,**d**) contain two methoxy groups decorating each 2-nitrobenzyloxycarbonyl fragment. The presence of these groups increases the sensitivity of the photoactivatable dyes to irradiation with 405 nm laser. The photophysical properties of all compounds are discussed in the next section.

The polarity of compounds **1b–d** was also assessed by measuring logP values (Figure S1); they were in the same range as for compound **1a** (1.6–2.0). The HaloTag analogues **11b–d** also showed similar hydrophilic properties as **11a** (logP ≈4); all values within the desired range to predict a good cell permeability (moderate logP values in the −0.5 to 5 range), according to the Lipinski's Rule of 5 (Ro5),[16] a popular guideline for drug and fluorescent probe design.[17] Therefore, we considered unnecessary the incorporation of morpholides in this case, to avoid an increase in the molecular mass, a property also considered to affect cell permeability by the Ro5.

For the synthesis of photoactivatable rhodamine 515R,[15c] as well as carborhodamines 560CP and 580CP,[15a,b] ditriflates **8b–d** were prepared according to the literature.[15a,18–20] The palladium-catalyzed double Buchwald–Hartwig amidation of ditriflates **8b–d** with carbamates (**9b–c**) afforded dye esters **10b–d** with photocleavable carbamate groups.[6a,21] The pendant *tert*-butyl ester groups were cleaved with trifluoroacetic acid (TFA) to obtain photoactivatable dyes **1b–e** carrying 5(6)-COOH groups suitable for conjugation. The amides were prepared from compounds **1b–d** and HaloTag™ amine (O2), as a recog-

nition unit readily binding with HaloTag fusion proteins (Scheme 3).

Photochemical and photophysical properties of photoactivatable dyes

We investigated the photochemical and photophysical properties of all five caged dyes as free carboxylic acids (**1a**–**e**). First, we examined the photoactivation of the caged α-carboxamide Q-SiR (**1a**) dissolved in acetonitrile—aq. buffer (1:1), to provide full solubility of the starting compound and the photolysis products. Irradiation with 365 nm light results in a significant increase of the absorption and fluorescence emission in the visible region, indicating the conversion into the fluorescent product(s) (Figure S2). The absorption transients produce an excellent fit to a double exponential function, suggesting a simple consecutive reaction scheme with one non-emissive intermediate.[10]

Small volumes of the irradiated mixture were detached at certain times and submitted to LC–MS analysis in order to validate the mechanism and unambiguously assign each kinetic constant to the corresponding step. Only three reactants were found: the initial compound ($m/z = +1081$), the single-caged intermediate ($m/z = +789$) and the final fluorescent and fully uncaged product ($m/z = +497$). From a global fit, the two kinetic constants and thus the reaction quantum yields for the consecutive steps were extracted, under assumption that the absorption coefficient of the intermediate is one half of that of the starting compound at the irradiation wavelength (365 nm). In HPLC, the acidic buffer (0.1 % w/w formic acid in aq. acetonitrile) fully transforms the final product to the colored open-ring form, but the intermediate with one caging group exists as a completely closed-ring isomer, even at such acidic conditions. However, under irradiation conditions (pH = 7), the absorption spectra indicate that the final product is at equilibrium between the open- (colored) and closed-ring (colorless) forms (see Supp. Inf.), due to the high acetonitrile content. Similar results were found for compounds **1b** and **1c** (Figures S3 and S4, and Table 1). For compound **1d**, a more complex activation mechanism was required to explain the absorption and emission transients in the visible range (Figure S5). In addition to the starting compound ($m/z = +917$), the mono-caged intermediate ($m/z = +678$), and the uncaged product ($m/z = +497$), two other intermediates with the same mass ($m/z = +678$) (isomers due to molecular asymmetry and hindered rotation across NR_2-CO bond) and displaying the same transients were found. With this more complicated reaction scheme involving four reaction constants (k_r), LC–MS data and complete sets of absorption transients produced reasonable fits. To summarize, all five studied caged compound showed clean photoreactions to the brightly fluorescent desired photoproducts (see Figures S2-S6). Importantly, despite the low absorption coefficients at 405 nm found for all caged compounds (especially **1a** and **1c**), activation was possible at this wavelength in diverse commercial microscopes. The introduction of the branching point and the morpholide residues results in reduced activation rates. The detailed spectral, photochemical and photophysical properties of the initial caged dyes, including model compound **1e** (Figure S6), and fluorescent products are given in Table 1.

Bioimaging

Photoactivatable fluoresceins,[7,12] rhodamines,[8b,9c] and Q-SiR[6b] masked by the presence of 2-nitrobenzyl(oxycarbonyl) residues have already been used in confocal and PALM/STORM imaging. Here we introduce photoactivatable carborhodamines **1b**,**c** and apply them, together with masked Q-SiR dye (**1a**) and rhodamine 515R (**1d**), in a cellular environment as substrates for Halo-Tag fusion proteins (compounds **11a–d**). We first tested the cell permeability of these reactive compounds, optimizing the labeling protocol on U2OS cells stably expressing vimentin-HaloTag fusion protein. The best conditions minimizing unspecific binding of the dye to endosomal structures were found at a concentration of 100–300 nM of the HaloTag probes with incubation times of 12–16 h. A viability test was performed after incubation of the cells with the dyes, and it showed no significant difference with respect to a control group (Figure S7). These conditions are similar to those reported for other spontaneously blinking[22] or photoactivatable dyes[2b,23] used in superresolution microscopy. Confocal images of living cells before and after photoactivation with 365 nm light exhibit pronounced contrast, as well as high specificity of all derivatives (Figure S8, upper panel). The activation was performed by scanning the sample with a 365 nm laser-beam over several frames, until a plateau was

Table 1: Reaction parameters of the photochemical reactions. Extinction coefficients of the starting compound (ε_{SC}^{355nm}) and the reaction intermediate ($\varepsilon_{Int}^{355nm}$) at the irradiation the wavelength (365 nm); reaction quantum yields of the first (ϕ_1) and second step (ϕ_2) of a consecutive reaction mechanism, in CH_3CN/ aq. PBS buffer (1:1) at pH 7. Absorption (λ_{FP}^{Abs}) and emission (λ_{FP}^{Em}) maxima, fluorescence quantum yield (Φ_{Fluo}), and fluorescence lifetime (τ_{Fluo}) of the fluorescent (uncaged) products, measured in PBS (pH = 7.4) from ref. [10, 15a]-c.

Compound	ε_{SC}^{365nm} [$M^{-1}cm^{-1}$]	$\varepsilon_{SC}^{\lambda_{irr}} \times \phi_1$	$\varepsilon_{Int}^{\lambda_{irr}} \times \phi_2$	$\phi_1 \times 10^{-3}$	$\phi_2 \times 10^{-3}$	$\lambda_{FP}^{Abs}/\varepsilon_{FP}$ [$nm/M^{-1}cm^{-1}$]	λ_{FP}^{Em} [nm]/ (Φ_{Fluo})	τ_{Fluo} [ns]
1a	550	1.5	1.5	0.27	0.54	640[10]/77000	660/0.38	3.0
1b	6465	61.6	24.9	9.5	7.7	582[15a]/90000	607/0.69	3.6
1c	558	26.7	16.4	48.0	59.0	561[15b]/61000	588/0.76	4.2
1d	7526	36.9	17.4	4.9	4.6	515[15c]/56000	543/0.86	3.1
1e	589	30.4	9.6	51.6	32.8	n.d.	n.d.	n.d.

reached (Figure S8, lower panel) for the emission signal on an image obtained with the corresponding excitation and emission wavelengths of the dye (activation and imaging was alternated line by line). The transients of the signal over the activation frames displayed similar kinetics as the activation in bulk experiments in solution, and were fitted to the same double exponential model function (for compound **11d** a simplified double exponential was sufficient to fit the data). Despite its relatively high hydrophobicity (logP = 6.02), model compound **11e** was also cell permeable (Figures S9 and S10). However, a much higher unspecific labeling was observed, in particular evidenced by an accumulation in large endosomes (Figure S9b). STED images of vimentin filaments also suggest a poorer or incomplete labeling efficiency in comparison with compound **11a** (Figure S10). SMLM imaging with compounds **11a–d**, was also possible on living cells (Figure S12), in this case performing the activation with a 405 nm laser.

2D and 3D MINFLUX nanoscopy on fixed cells

Lastly, we assessed the applicability of the novel caged fluorophores in MINFLUX nanoscopy. To that end, we stained living U2OS cells expressing HaloTag protein on NUP96 with compounds **11a–c** and **11e**, using the same conditions optimized for staining the Vimentin-Halo construct, and then fixed the cells for imaging to prevent cell movements (see Figure S11 and Supplementary movies SM1 and SM2) over the image acquisition time (from 30 min up to overnight for large regions of interest [ROIs]). Live-cell labeling has advantages over labeling-after-fixation, as it enables, for example, pulse-chase experiments[24] and avoids possible artifacts introduced by inhibition of the tags by the fixatives.[25,26] In addition, our dyes may be candidates for (MINFLUX) tracking experiments involving photoactivatable dyes.[27] Imaging was performed on a commercial MINFLUX setup, equipped with 488 nm confocal excitation wavelength, 561 nm and 640 nm MINFLUX excitation wavelength, and activation at 405 nm. The available excitation wavelengths of the microscope exclude the use of **11d**, and therefore we did not attempt MINFLUX imaging with this compound. Counter labeling with commercially available WGA-Alexa Fluor 488 was used to find and focus on nuclei by confocal imaging. The use of this dye and its imaging in a confocal mode neither affect the target compounds, nor produce observable uncaging. In agreement with the photophysical measurements, compound **11b** required lower activation power (0.5 % laser power) for the appearance of first events than the other two compounds (5 % laser power). This activation power was gradually increased during the acquisition of the image, specifically up to 100 % for all samples at the end of the measurements to ensure that all probes had been photoactivated. Image acquisition was stopped when fluorescent events became too sparse in time. A low photoactivation quantum yield is a highly desirable property for imaging fixed samples as it permits good control over the activation of fluorophores and reduces the probability of double-activated events (i.e. two markers in the fluorescent form within a diffraction-limited spot). It also minimizes undesirable activation by the excitation laser around areas of maximum intensity of the excitation beam, potentially produced by the absorption of very weak hot bands of the caged compound.[28]

All samples were imaged in two dimensions (2D) with a modified imaging sequence requiring only 30 photons per iteration, which resulted in multiple localizations per molecule and decreased the probability of missing activated molecules. Subsequently, the localizations were processed according to previously described methods (see Supporting Information) for image rendering and analysis. Compounds **11a** (Figure 1), **11b** (Figure S13), **11c** (Figure S14) and **11e** (Figure S18) produced good quality images of NUPs, showing rings exposing the well-known 8-fold NUP symmetry,[29] with well-resolved corners. However, images with fully labeled NUP structures are harder to achieve with compound **11c** and **11e**. Analysis of final images (from Figure 1a, S13a, S14a and S18a) with identical parameters (for better comparison) resulted in a mean total of 6181, 2977, 2137 and 5300 photons detected per molecule in multiple localizations for compounds **11a**, **11b**, **11c** and **11e**, respectively. The analysis revealed a 2D localization precision of 2.2–2.3 nm for all compounds, remarkably with only 30 photons per localization (Figure S15 and S18). To further understand the differences in the imaging performance of these four compounds, the images were analyzed by using a modification of established procedures.[30] In brief, MINFLUX images were automatically segmented by a cross correlation with a ring-like structure (diameter = 100 nm) convoluted with a Gaussian (FWHM = 10 nm) to select NUP structures. Then, the positions of all localizations on each ROI were fitted to a circle function and centered according to the obtained value. An 8-bin histogram of the raw angular positions was used to extract an occupancy parameter that was defined as the average number of corners were at least one fluorophore was localized (Figure 2b–d). Mean occupancies of 6.6 (**11a**), 6.3 (**11b**), 4.5 (**11c**) and 5.4 (**11e**) were obtained. These numbers and the corresponding histograms (Figure S16a–c and S18g) are similar to the ones obtained in STORM imaging with the dye Alexa Fluor 647,[26] a blinking cyanine that unlike our caged compounds can be switched-on and detected more than once. In general, these results account for the adequacy and "completeness" of the NUP images acquired. To shed more light on the observed differences, we counted the total number of activated single fluorophores (TIDs) per NUP and obtained average of values of 17, 36, 8, and 11, respectively (Figure S16d–f and S18h). Because there are four protein copies per corner (32 in total expected per NUP in a 2D projection),[29] we can conclude that the combined labeling and detection efficiency of compound **11a** is approximately 53 %.

This is superior to the value obtained with HaloTag reactive adducts of cyanines (20–40 %) or DNA-PAINT (ca. 30 %),[30c] but lower to the best achieved values reported with nanobody labeling strategies combining two clones (60–70 %).[30] In the other extreme, the poor 25–35 % efficiency of compounds **11c–11e** explains the lower image quality, in

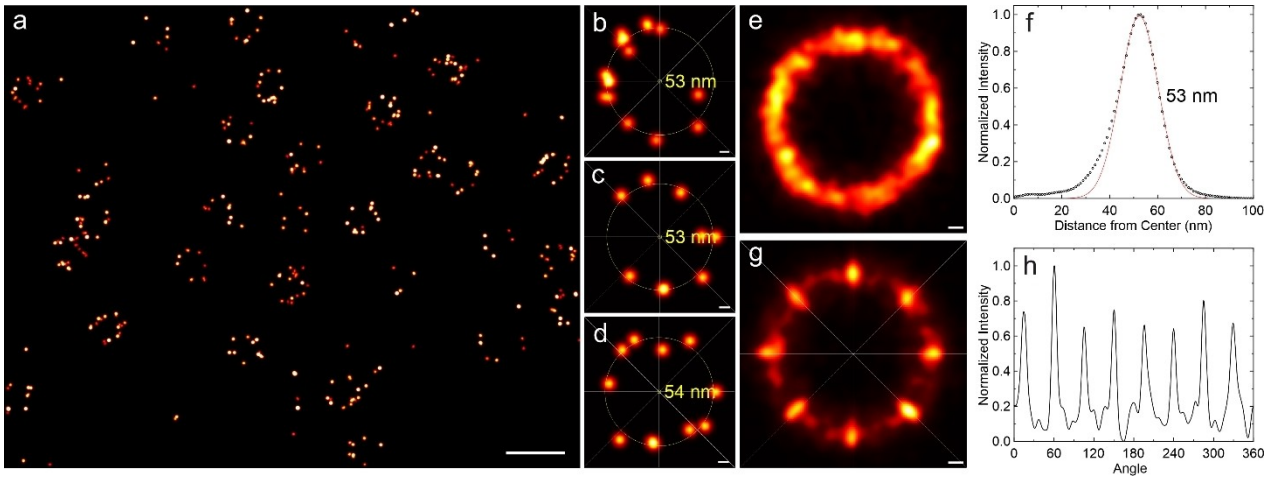

Figure 1. (a) Minflux image of fixed U2OS cells stably expressing NUP96-HaloTag, labeled with compound **11a** (250 nM). (b–d) Selected NUPs, centered and with the corresponding circle fits (yellow lines, indicated fitted radius). (e) Rendered image after registration of 345 selected NUPs (from 8 different cells/ROIs). (f) Average radial profile of the image in (e), along with a Gaussian fit (the calculated radius is shown). (g) Image rendered after rotational alignment of the localizations of the 345 NUPs, after an angle randomization with the only assumption of an 8-fold symmetry. (h) Circle profile around the calculated mean radius ($R_{AV}=53$ nm) and averaged at $R=R_{AV}\pm5$ nm. Scale bars: (a) 200 nm, (b, c, d, e, f) 10 nm.

terms of NUP "completeness". Compound **11b** shows a higher average value of detections. However, the observation of a large number of cases with over 32 SM detections and the lower corner occupancy compared to compound **11a** suggest that the activated fluorophore (580CP) may blink in the mounting medium used (PBS), with relatively long off times. This would result in an overestimation of the obtained value by erroneously counting the same marker two or more times. Importantly, we neither apply any background correction on the images, nor on the selected NUP ROIs submitted to analysis, since the images only show few off-targeted localizations. The positions of all selected NUPs, corrected by the center position obtained from the circle-function fit, were used to generate an average superresolution image of the equivalent "superparticle" (Figure 1e, S13e, S14e and S18d), and its average radial profile (Figure 1f, S13f, S14f and S18f). From a Gaussian fitting, we obtained an average radius $R_{AV}=53$ nm with the four compounds, in agreement with the previously reported values for NUP96, measured by STORM with a NUP96-SNAP construct labeled with SNAP-AF647 (53.7 nm),[26] or by MINSTED with a NUP96-GFP construct labeled with an anti-GFP nanobody containing a DNA binding site for hybridization with a complementary strand labeled with Cy3B (55.5 nm).[3b] Alternatively, the average radius was obtained from a circle fit to the localization positions, giving values of 53.4 nm, 53.1 nm, 52.8 nm and 52.9 nm (all values with standard deviation of 3 nm) for compounds **11a**, **11b**, **11c** and **11e**, respectively (Figure S17 and S18i). Furthermore, we applied a rotational alignment of the centered NUP localizations to align them by the angle with the maximum amount of localizations, followed by an angle randomization to eliminate the "hot spot" artifact.[31] The final image obtained from the average of 345 NUPs exposes the 8-fold symmetry (Figure 1g, S13g and S14g), evidenced by a large contrast in the intensity radial profile (Figure 1h, S13h and S14h), calculated at $R_{AV}\pm5$ nm (averaged at 1 nm steps).

Summarizing, compounds **11a** and **11e** produce a large mean value of photons/molecule (over 5000 photons), higher than compounds **11b–c**, (2000–3000) reflecting the higher fatigue resistance of red-emitting dyes, in particular of silicon rhodamines over their (carbo)rhodamine counterparts. The mean occupancy is expected to represent the combined labeling and detection efficiency. The values observed correlates with the trend in measured hydrophilicity (logP) and thus seems to be mostly influenced by changes in labeling efficiencies, with the exception of **11c** showing an unexpectedly low occupancy. With **11c** presenting the lowest fatigue resistance (i.e. lower photons/molecule value) of all compounds, we attribute its low occupancy to poor detection efficiency, rather than incomplete labeling. Altogether, compound **11a** has a superior overall performance than the rest of the markers.

Encouraged by these results, we selected compound **11a** for 2D and 3D MINFLUX imaging vimentin filaments, of a cellular structure with markedly different characteristics. To that end, U2OS cells expressing HaloTag protein on vimentin were labeled and imaged under the same conditions that were used for imaging NUP96. First, a 2D image of filaments in a flat and relatively thin area of the cell was acquired (Figure 2a–c). A localization precision of 2.2 nm was achieved in good agreement with the images obtained with NUPs. Line profiles were measured perpendicularly to manually selected single filaments, and their FHWM calculated by Gaussian fits. An average width of 12 ± 2 nm (from a total of ten filaments) was obtained, which is in good agreement with cryo-electron tomography data.[32] 2D MINFLUX images vimentin filaments on live cells were acquired as a proof of principle (Figure S19), on very small

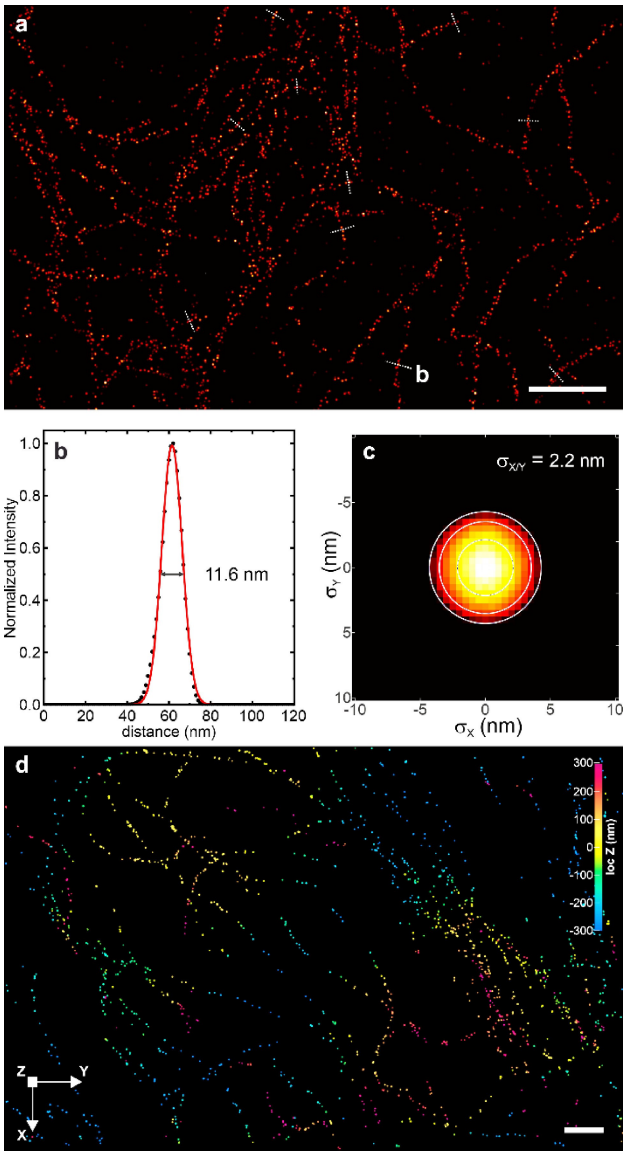

Figure 2. (a) 2D MINFLUX image of fixed U2OS cells expressing Vimentin-HaloTag construct labelled with compound **11a** (250 nM, 16 h). The average width of vimentin filaments was calculated from the dashed lines. (**b**) A line profile and calculated filament width, showing the processed MINFLUX data points along with the Gaussian fit (red line). (**c**) 2D dispersion of localizations in (a). (d) 3D MINFLUX image of fixed U2OS cells expressing Vimentin-HaloTag construct labelled with compound **11a** (250 nM, 16 h). Localizations were binned to 500 photons/localization and filtered prior to rendering (for details, see SI) The corresponding unbinned data was used to render Video S1. Scale bars: 500 nm.

ROIs and for short acquisition times. The movement of the filaments during acquisition for 2 min is evident, and corroborates the expectation from confocal and STED time-lapse images. This experiment demonstrates the feasibility of using compound **11a** for live-cell experiments in a MINFLUX microscope. Next, a thicker area of the cell in close proximity of the nucleus were chosen for imaging in 3D mode, to assess the fluorophore performance over a broad axial range and in much denser conditions than that offered by imaging nuclear pores. The 3D image of vimentin filaments was rendered and animated (Video S1), demonstrating high quality localizations in an axial range of 0.6 µm. With only 30 photons per localization, axial and lateral localization precisions of 3.2 and 3.8 nm were achieved, respectively (Figure S20). The localizations along the filaments in 2D and 3D (Figure 2a, d) images are sparse, however the sparsity is not attributed to missing labels. Two main reasons account for this observation. Firstly, the natural structure of vimentin filaments shows an organization pattern with a repetition of alternating 10 and 39 nm distances,[33] which is significantly larger than our localization precision. Secondly, the U2OS cell line used is monoclonal heterozygous;[19] hence, not every vimentin expressed is fused to a HaloTag protein, with a considerably larger proportion of non-fused protein. The 3D imaging demonstrated that the continuity of filaments decreases with the increasing distance from the z-origin, most likely due to aberrations in the donut-shaped excitation intensity profile of the MINFLUX system. However, it was sufficient for visualizing filaments about 300 nm above and below the selected focal plane. Nevertheless, the mean total number of photons per molecule (from multiple localizations) calculated from the 3D image was 6406, which is similar to the 2D image of NUP96 acquired with the same compound. Thus, to improve the localization precision and the image quality, multiple localizations were binned to 500 photons/localization (Figure 2d). After applying the same filters (i.e. localizations with low photons or outside a z-range; see SI), the localization precision in all three dimensions was improved to 1.6 nm (Figure S21). To our knowledge, this is the first 3D-MINFLUX image of vimentin filaments, demonstrating the superior properties of the compound **11a** for 3D-imaging areas with a large density of structures and markers.

Conclusion

Up to now, the majority of organic dyes applied in MINFLUX nanoscopy belongs to the class of "blinking" cyanines, such as Alexa Fluor 647, that are cell-impermeable due to the presence of multiple negatively charged groups and incompatible with live-cell imaging. The latter feature relates to the necessity of using high concentrations of thiols and oxygen scavenger buffers for efficient blinking. In contrast, photoactivatable dyes emerge as a viable alternative to cyanines,[6a,23] because they do not require the presence of any special medium or dedicated conditions to perform (other than light). Our study dealt with (minimal) requirements expected for the cell-permeable photoactivatable dyes: specific live-cell labeling, clean photoactivation and viable 2D- and 3D-imaging on a MINFLUX setup (561 nm or 640 nm excitation and 405 nm photoactivation lasers).

HaloTag fusion proteins were chosen as targets in living cells due to their fast and irreversible reaction with the probes incorporating ω-haloalkane residues. Other protein tags may require higher concentrations of the probes, due to

slower reaction rates or non-covalent binding character. Successful labeling and imaging in confocal and SMLM microscopes were achieved with all four probes, on live cells and without any additives. Four dyes (**11a**—**c**, **11e**) were shown to be applicable and compatible with the acquisition procedure of the standard MINFLUX setup, though their performance was different. The far-red emitting cage marker (**11a**) produced outstanding results in terms of labeling completeness and photostability, comparable to previously established dyes (cyanines) delivering over 6000 photons on average per activated single molecule. Compounds **11b**–**c** delivered 2000–3000 photons, also allowing single-digit localization precision, but with lower labeling efficiency.

The clean reaction and full conversion of all compounds **1a**–**d** into fluorescent dyes are important features which justify further use of [(2-nitrobenzyl)oxy]carbonyl group.[12] We also demonstrated the utility of α-carboxyl group as a branching point to introduce additional functionalities. In our case, a morpholine unit was introduced at this position to increase the hydrophilicity and impart cell permeability for the bulky and rigid polycyclic Q-SiR core. If required, other functionalities may be introduced at this position without changing the spectral properties of the dye. The relatively low values of the photoactivation quantum yields (0.3–6 %, tunable by the presence of methoxy groups in the nitrobenzene ring) are advantageous for MINFLUX imaging on densely labeled areas, as these dyes are not readily photoactivated by the relatively strong excitation source. We expect that the photoactivatable caged fluorophores presented in this work (in particular **11a**), with their high labeling efficiency, reliable and controllable activation, high brightness and photostability of the fluorescent products, will contribute to the exploration of complex biological objects by 3D-MINFLUX nanoscopy.[33,34]

Acknowledgements

The research was funded by Bundesministerium für Bildung und Forschung (German Federal Ministry of Education and Research), project no. 13N14122 "3D Nano Life Cell" (S.W.H.). We thank S. Jakobs (MPI-NAT) for providing the U2OS-Vim-Halo and the EMBL for providing the U2OS-NUP96-Halo cells. We also thank our colleagues at the Department of Optical Nanoscopy—J. Hubrich and A. Fischer—for supporting the cell culture and cell viability tests, Dr. M. Remmel and Dr. J. Engelhardt—for providing access to the PALM setup, and Dr. E. D'Este (Optical Microscopy Facility, MPI-MF)—for the access to the confocal, STED and MINFLUX setups. We thank J. Bienert (MPI NAT) for performing analyses of the dyes and intermediates. Open Access funding enabled and organized by Projekt DEAL.

Conflict of Interest

The authors declare no conflict of interest.

Data Availability Statement

The data that support the findings of this study are available in the supplementary material of this article.

Keywords: Dyes/Pigments · Fluorescence · Photolysis · Single-Molecule Photoactivation · Superresolution Microscopy

[1] a) S. J. Sahl, S. W. Hell, S. Jakobs, *Nat. Rev. Mol. Cell Biol.* **2017**, *18*, 685–701; b) "Far-Field Optical Nanoscopy": Springer Series on Fluorescence (Methods and Applications), *Vol. 14* (Eds.: P. Tinnefeld, C. Eggeling, S. W. Hell), Springer, Berlin, **2012**; c) Y. M. Sigal, R. Zhou, X. Zhuang, *Science* **2018**, *361*, 880–887.

[2] a) K. C. Gwosch, J. K. Pape, F. Balzarotti, P. Hoess, J. Ellenberg, J. Ries, S. W. Hell, *Nat. Methods* **2020**, *17*, 217–224; b) J. K. Pape, T. Stephan, F. Balzarotti, R. Büchner, F. Lange, D. Riedel, S. Jakobs, S. W. Hell, *Proc. Natl. Acad. Sci. USA* **2020**, *117*, 20607–20614; c) M. Remmel, L. Scheiderer, A. N. Butkevich, M. L. Bossi, S. W. Hell, *Small* **2023**, *19*, 2206026.

[3] a) M. Weber, M. Leutenegger, S. Stoldt, S. Jakobs, T. S. Mihaila, A. N. Butkevich, S. W. Hell, *Nat. Photonics* **2021**, *15*, 361–366; b) M. Weber, H. Von der Emde, M. Leutenegger, P. Gunkel, S. Sambandan, T. A. Khan, J. Keller-Findeisen, V. C. Cordes, S. W. Hell, *Nat. Biotechnol.* **2023**, *41*, 569–576.

[4] a) L. M. Wysocki, L. D. Lavis, *Curr. Opin. Chem. Biol.* **2011**, *15*, 752–759; b) M. Sauer, M. Heilemann, *Chem. Rev.* **2017**, *117*, 7478–7509; c) H. Li, J. C. Vaughan, *Chem. Rev.* **2018**, *118*, 9412–9454; d) "Photoswitchable Fluorophores for Super-Resolution Optical Microscopy": K. Uno, V. N. Belov, M. L. Bossi, in *Molecular Photoswitches, Vol. 2* (Ed.: Z. L. Pianowski), Wiley-VCH, Weinheim, **2022**, pp. 605–626.

[5] a) M. J. Rust, M. Bates, X. Zhuang, *Nat. Methods* **2006**, *3*, 793–795; b) E. Betzig, G. H. Patterson, R. Sougrat, O. W. Lindwasser, S. Olenych, J. S. Bonifacino, M. W. Davidson, J. Lippincott-Schwartz, H. F. Hess, *Science* **2006**, *313*, 1642–1645; c) S. T. Hess, T. P. K. Girirajan, M. D. Mason, *Biophys. J.* **2006**, *91*, 4258–4272.

[6] a) A. N. Butkevich, M. Weber, A. R. C. Delgado, L. M. Ostersehlt, E. D'Este, S. W. Hell, *J. Am. Chem. Soc.* **2021**, *143*, 18388–18393; b) J. B. Grimm, T. Klein, B. G. Kopek, G. Shtengel, H. F. Hess, M. Sauer, L. D. Lavis, *Angew. Chem. Int. Ed.* **2016**, *55*, 1723–1727; *Angew. Chem.* **2016**, *128*, 1755 - 1759; c) H. Kashima, M. Kamiya, F. Obata, R. Kojima, S. Nakano, M. Miurab, Y. Urano, *Chem. Commun.* **2021**, *57*, 5802–5805.

[7] S. Hauke, A. von Appen, T. Quidwai, J. Ries, R. Wombacher, *Chem. Sci.* **2017**, *8*, 559–566.

[8] a) S. Banala, D. Maurel, S. Manley, K. Johnsson, *ACS Chem. Biol.* **2012**, *7*, 289–293; b) D. Maurel, S. Banala, T. Laroche, K. Johnsson, *ACS Chem. Biol.* **2010**, *5*, 507–516.

[9] a) G. Y. Mitronova, V. N. Belov, M. Bossi, C. Wurm, L. Meyer, R. Medda, G. Moneron, S. Bretschneider, C. Eggeling, S. Jakobs, S. W. Hell, *Chem. Eur. J.* **2010**, *16*, 4477–4488; b) K. Kolmakov, V. N. Belov, C. A. Wurm, B. Harke, M. Leutenegger, C. Eggeling, S. W. Hell, *Eur. J. Org. Chem.* **2010**, 3593–3610; c) L. M. Wysocki, J. B. Grimm, A. N. Tkachuk, T. A. Brown, E. Betzig, L. D. Lavis, *Angew. Chem. Int. Ed.* **2011**, *50*, 11206–11209; *Angew. Chem.* **2011**, *123*, 11402 – 11405.

[10] M. Weber, T. A. Khan, L. J. Patalag, M. Bossi, M. Leutenegger, V. N. Belov, S. W. Hell, *Chem. Eur. J.* **2021**, *27*, 451–458.

[11] D. Puliti, D. Warther, C. Orange, A. Specht, M. Goeldner, *Bioorg. Med. Chem.* **2011**, *19*, 1023–1029.

[12] a) T. J. Mitchison, K. E. Sawin, J. A. Theriot, K. Gee, A. Mallavarapu, *Methods Enzymol.* **1998**, *291*, 63–78; b) T. Milburn, N. Matsubara, A. P. Billington, J. B. Udgaonkar,

J. W. Walker, B. K. Carpenter, W. W. Webb, J. Marque, W. Denk, J. A. McCray, G. P. Hess, *Biochemistry* **1989**, *28*, 49–55; c) K. R. Gee, R. Wieboldt, G. P. Hess, *J. Am. Chem. Soc.* **1994**, *116*, 8366–8367; d) K. R. Harwood, S. C. Miller, *ChemBioChem* **2009**, *10*, 2855–2857; e) F. M. Rossi, M. Margulis, C.-M. Tang, J. P. Y. Kao, *J. Biol. Chem.* **1997**, *272*, 32933–32939.

[13] A. P. Kourounakis, D. Xanthopoulos, A. Tzara, *Med. Res. Rev.* **2020**, *40*, 709–752.

[14] a) R. P. Haugland, US Pat. 5,635,608, **1997**; b) L. M. van Langen, R. P. Selassa, F. van Rantwijk, R. A. Sheldon, *Org. Lett.* **2005**, *7*, 327–329.

[15] a) A. N. Butkevich, G. Y. Mitronova, S. C. Sidenstein, J. L. Klocke, D. Kamin, D. N. H. Meineke, E. D'Este, P.-T. Kraemer, J. G. Danzl, V. N. Belov, S. W. Hell, *Angew. Chem. Int. Ed.* **2016**, *55*, 3290–3294; *Angew. Chem.* **2016**, *128*, 3350 – 3355; b) A. N. Butkevich, V. N. Belov, K. Kolmakov, V. V. Sokolov, H. Shojaei, S. C. Sidenstein, D. Kamin, J. Matthias, R. Vlijm, J. Engelhardt, S. W. Hell, *Chem. Eur. J.* **2017**, *23*, 12114–12119; c) F. Grimm, S. Nizamov, V. N. Belov, *ChemBioChem* **2019**, *20*, 2248–2254.

[16] C. A. Lipinski, F. Lombardo, B. W. Dominy, P. J. Feeney, *Adv. Drug Delivery Rev.* **2001**, *46*, 3–26.

[17] a) K. Soliman, F. Grimm, C. A. Wurm, A. Egner, *Sci. Rep.* **2021**, *11*, 6991; b) S. H. Alamudi, R. Satapathy, J. Kim, D. Su, H. Ren, R. Das, L. Hu, E. Alvarado-Martínez, J. Y. Lee, C. Hoppmann, E. Peña-Cabrera, H.-H. Ha, H.-S. Park, L. Wang, Y.-T. Chang, *Nat. Commun.* **2016**, *7*, 11964.

[18] J. B. Grimm, A. J. Sung, W. R. Legant, P. Hulamm, S. M. Matlosz, E. Betzig, L. D. Lavis, *ACS Chem. Biol.* **2013**, *8*, 1303–1310.

[19] A. N. Butkevich, H. Ta, M. Ratz, S. Stoldt, S. Jakobs, V. N. Belov, S. W. Hell, *ACS Chem. Biol.* **2018**, *13*, 475–480.

[20] W.-C. Sun, K. R. Gee, D. H. Klaubert, R. P. Haugland, *J. Org. Chem.* **1997**, *62*, 6469–6475.

[21] J. B. Grimm, L. D. Lavis, *Org. Lett.* **2011**, *13*, 6354–6357.

[22] a) S.-N. Uno, M. Kamiya, T. Yoshihara, K. Sugawara, K. Okabe, M. C. Tarhan, H. Fujita, T. Funatsu, Y. Okada, S. Tobita, Y. Urano, *Nat. Chem.* **2014**, *6*, 681–689; b) J. Tyson, K. Hu, S. Zheng, P. Kidd, N. Dadina, L. Chu, D. Toomre, J. Bewersdorf, A. Schepartz, *ACS Cent. Sci.* **2021**, *7*, 1419–1426.

[23] R. Lincoln, M. L. Bossi, M. Remmel, E. D'Este, A. N. Butkevich , S. W. Hell, *Nat. Chem.* **2022**, *14*, 1013–1020.

[24] a) M. F. Mossuto, S. Sannino, D. Mazza, C. Fagioli, M. Vitale, E. Yoboue, R. Sitia, T. Anelli, *PLoS One* **2014**, *9*, e108496; b) H. Wang, Y.-P. Lin, C. Mitchell, S. Ram, J. O'Brien, *J. Cell Sci.* **2015**, *128*, 3888–3897.

[25] D. R. Whelan, T. D. M. Bell, *Sci. Rep.* **2015**, *5*, 7924.

[26] J. V. Thevathasan, M. Kahnwald, K. Cieśliński, P. Hoess, S. K. Peneti, M. Reitberger, D. Heid, K. C. Kasuba, S. J. Hoerner, Y. Li, Y.-L. Wu, M. Mund, U. Matti, P. M. Pereiro, R. Henriques, B. Nijmeijer, M. Kueblbeck, V. J. Sabinina, J. Ellenberg, J. Ries, *Nat. Methods* **2019**, *16*, 1045–1053.

[27] a) S. Manley, J. Gillette, G. Patterson, H. Shroff, H. Hess, E. Betzig, J. Lippincott-Schwartz, *Nat. Methods* **2008**, *5*, 155–157; b) T. Deguchi, M. Iwanski, E.-M. Schentarra, C. Heidebrecht, L. Schmidt, J. Heck, T. Weihs, S. Schnorrenberg, P. Hoess, S. Liu, V. Chevyreva, K.-M. Noh, L. Kapitein, J. Ries, *Science* **2023**, *379*, 1010–1015.

[28] a) J. L. Clark, P. F. Miller, G. Rumbles, *J. Phys. Chem. A* **1998**, *102*, 4428–4437; b) Y. Liu, Q. Su, X. Zou, M. Chen, W. Feng, Y. Shi, F. Li, *Chem. Commun.* **2016**, *52*, 7466–7469; c) R. Kashihara, M. Morimoto, S. Ito, H. Miyasaka, M. Irie, *J. Am. Chem. Soc.* **2017**, *139*, 16498–16501; d) X. Zhu, Q. Su, W. Feng, F. Li, *Chem. Soc. Rev.* **2017**, *46*, 1025–1039; e) T. Gajdos, B. Hopp, M. Erdélyi, *J. Fluoresc.* **2020**, *30*, 437–443; f) K. Uno, A. Aktalay, M. L. Bossi, M. Irie, V. N. Belov, S. W. Hell, *Proc. Natl. Acad. Sci. USA* **2021**, *118*, e2100165118.

[29] A. von Appen, J. Kosinski, L. Sparks, A. Ori, A. L. DiGuilio, B. Vollmer, M.-T. Mackmull, N. Banterle, L. Parca, P. Kastritis, K. Buczak, S. Mosalaganti, W. Hagen, A. Andres-Pons, E. A. Lemke, P. Bork, W. Antonin, J. S. Glavy, K. H. Bui, M. Beck, *Nature* **2015**, *526*, 140–143.

[30] a) A. Löschberger, S. Van de Linde, M.-C. Dabauvalle, B. Rieger, M. Heilemann, G. Krohne, M. Sauer, *J. Cell Sci.* **2012**, *125*, 570–575; b) A. Szymborska, A. De Marco, N. Daigle, V. C. Cordes, J. A. G. Briggs, J. Ellenberg, *Science* **2013**, *341*, 655–658; c) T. Schlichthaerle, M. T. Strauss, F. Schueder, A. Auer, B. Nijmeijer, M. Kueblbeck, V. J. Sabinina, J. V. Thevathasan, J. Ries, J. Ellenberg, R. Jungmann, *Angew. Chem. Int. Ed.* **2019**, *58*, 13004–13008; *Angew. Chem.* **2019**, *131*, 13138 – 13142.

[31] a) H. Heydarian, F. Schueder, M. T. Strauss, B. van Werkhoven, M. Fazel, K. A. Lidke, R. Jungmann, S. Stallinga, B. Rieger, *Nat. Methods* **2018**, *15*, 781–784; b) V. J. Sabinina, M. J. Hossain, J.-K. Hériché, P. Hoess, B. Nijmeijer, S. Mosalaganti, M. Kueblbeck, A. Callegari, A. Szymborska, M. Beck, J. Ries, J. Ellenberg, *Mol. Biol. Cell* **2021**, *32*, 1523–1533.

[32] M. Eibauer, M. S. Weber, Y. Turgay, S. Sivagurunathan, R. D. Goldman, O. Medalia, *bioRxiv preprint* **2021**, https://doi.org/10.1101/2021.07.15.452584.

[33] F. N. Vicente, M. Lelek, J.-Y. Tinevez, Q. D. Tran, G. Pehau-Arnaudet, C. Zimmer, S. Etienne-Manneville, G. Giannone, C. Leduc, *Sci. Adv.* **2022**, *8*, eabm2696.

[34] L. M. Ostersehlt, D. C. Jans, A. Wittek, Jan K. -Findeisen, K. Inamdar, S. J. Sahl, S. W. Hell, S. Jakobs, *Nat. Methods* **2022**, *19*, 1072–1075.

Manuscript received: February 23, 2023
Accepted manuscript online: August 9, 2023
Version of record online: ■■, ■■

Research Articles

Fluorescent Probes

A. Aktalay, T. A. Khan, M. L. Bossi,*
V. N. Belov,* S. W. Hell* —— **e202302781**

Photoactivatable Carbo- and Silicon-Rhodamines and Their Application in MINFLUX Nanoscopy

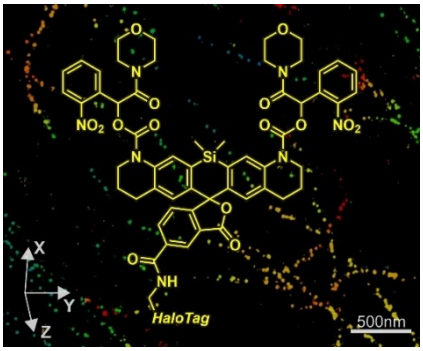

Optical nanoscopy of cells expressing Vimentin-HaloTag fusion proteins and labeled with photoactivatable fluorescent dyes is demonstrated in 2D and 3D modes on a commercial MINFLUX (minimal fluxes) setup. The dye synthesis and properties, photoactivation rates, labeling procedures, detection efficiencies, and other parameters related to the practical use of the probes are reported and discussed.